https://doi.org/10.1016/j.enconman.2018.05.100

Numerical modeling of a cogeneration system based on a direct carbon solid oxide fuel cell and a thermophotovoltaic cell

Zhimin Yang[1, §], Haoran Xu[2, 3, §], Bin Chen[3], Peng Tan[3], Houcheng Zhang[2, *], Meng Ni[3, *]

[1]Department of Physics, Xiamen University, Xiamen 361005, China

[2]Department of Microelectronic Science and Engineering, Ningbo University, Ningbo 315211, China

[3]Department of Building and Real Estate, The Hong Kong Polytechnic University, Hung Hom, Kowloon, Hong Kong, China

Abstract: A new combined system model is proposed to numerically assess the feasibility and effectiveness of using a thermophotovoltaic cell (TPVC) for waste heat recovery from a direct carbon solid oxide fuel cell (DC-SOFC). The system model mainly consists of an irreversible TPVC model and a 2D tubular DC-SOFC model considering the ionic/electronic charge transport, mass transport, momentum transport, and chemical/electrochemical reactions. Mathematical expressions of the power density and efficiency for the proposed system are derived and the performance characteristics of the combined system are revealed. The impacts of operation conditions and designing parameters including the operating temperature of the DC-SOFC, distance between the carbon layer and anode, and band-gap energy of the TPVC on the combined system performance are examined. It is found that the TPVC can efficiently harvest the waste heat from the DC-SOFC. The maximum power density of the combined system is approximately 56.2% larger than that of the stand-alone DC-SOFC. Moreover, a higher operating temperature of the DC-SOFC and a smaller distance between the carbon layer and the anode are beneficial to the performance enhancement of the combined system. The power density of the combined system can be further improved through designing the TPVC with an optimum band gap.

Keywords: Direct carbon solid oxide fuel cell, Waste heat recovery, Thermophotovoltaic cell, Combined system, Numerical modeling

[§] These two authors contribute equally to this work.

[*] Corresponding authors.

Email addresses: zhanghoucheng@nbu.edu.cn (H. Zhang); bsmengni@polyu.edu.hk (M. Ni).

1. Introduction

With the increasing fossil fuels depletion and energy demand, considerable efforts have been devoted to exploring renewable energy sources such as solar energy, wind energy, and fuel cells [1]. Compared with solar and wind energy, fuel cells are capable of directly converting the chemical energy of fuel into electricity and are efficient, reliable, and durable [2-4]. Most kinds of fuel cells use hydrogen as fuel but the large-scale hydrogen production suffers from some technological hurdles [5].

Different from hydrogen-fueled fuel cells, direct carbon fuel cells (DCFCs) use solid carbon fuel for power generation at high temperatures (typically ~800℃) [6, 7]. According to the types of electrolyte, DCFCs can be classified into three kinds: molten carbonate, molten hydroxide, and solid oxide DCFCs. Thereinto, the direct carbon solid oxide fuel cells (DC-SOFCs) are more suitable DCFCs because of their all-solid structure and non-noble metal catalysts [6]. It has been revealed that the performance of the DC-SOFC closely relies on the operation conditions and design parameters. Johnson et al. [8] analyzed the impacts of the design parameters including the tube spacing, carbon bed height, and cell voltage on the power density and efficiency of a solid oxide-based tubular air carbon fuel cell using the finite element method. It was found that the power density increases while the efficiency decreases with the increase of the bed height or tube spacing. Moreover, the DC-SOFC performance is also significantly affected by the carbon gasification kinetics [9]. Li et al. [10] experimentally studied the impacts of various catalysts on the performance of the DC-SOFC. Among K, Ni and Ca, K shows the best catalytic effect for carbon black gasification, while Ca exhibits the poorest catalytic effect for carbon black gasification. The effects of various kinds of carbon on the performance of the DC-SOFC were also found to be different. Jewulski et al. [11] investigated the lignite and char derived from lignite as fuel for the DC-SOFC. It was found that the

DC-SOFC performance using char as fuel is better than that using lignite as fuel. Furthermore, the DC-SOFC usually operates at high temperatures so that the mass transport and thermal effect inside the cell should be also considered. Xu et al. developed a multi-physics model considering the electrochemical reaction, chemical reactions, ionic/electronic charge transport, mass transport and momentum transport to investigate the performance characteristics [12] and thermal effect [13] of a tubular DC-SOFC. It was found that the molar fraction of CO at the anode can be tuned by operating conditions, and the effect of the cell length on the current density of the DC-SOFC was weak. Similar to the other high-temperature fuel cells, excessive heat can be generated in the DC-SOFC when the DC-SOFC is operated at a high current density. The overall efficiency of the fuel cell system can be further enhanced if the excessive heat generated is further harvested by various approaches including thermoelectric generator (TEG) [14], thermionic converter (TIC) [15], thermophotovoltaic cell (TPVC) [16], gas turbine (GT) [17], Stirling cycle [18], Brayton cycle [19], etc [20]. The TPVC is a solid-state generator and enables to directly convert heat into electricity, which offers advantages such as silent, efficient, and clean [21]. Yang et al. [22] compared the above several technologies for waste heat recovery from the molten carbonate fuel cells (MCFCs) and found that the TPVC was more efficient than the other waste heat recovery technologies, as shown in Fig. 1. Obviously, the heat released from the DC-SOFC, if any, can be used to drive the TPVC for additional electricity production. Xu et al. [23, 24] used Stirling engine and Otto engine to harvest the waste heat from the 2D DC-SOFC and found that the proposed approaches could efficiently harvest the waste heat from the DC-SOFC. However, no study has been conducted to recover the waste heat from the DC-SOFC using the TPVC and the performance comparisons of available DC-SOFC-based combined systems are rarely reported.

In this study, a solid-state TPVC is put forwarded to harvest the possible waste heat from a 2D tubular

DC-SOFC. The adopted fuel cell model fully considers the ionic/electronic charge transport, mass transport, and momentum transport processes, which is more accurate than a black box fuel cell model before [14-22]. The output and thermal characteristics of the DC-SOFC are solved by finite element method. How to integrate these two subsystems and operate the combined system will be elaborated. The feasibility and effectiveness of this waste heat recovery technology will be evaluated. The impacts of operation conditions and designing parameters of the subsystems on the power density and efficiency of the combined system are discussed. The maximum power density is calculated and the optimal parameters are obtained. Finally, several DC-SOFC-based combined systems are compared. The obtained results may provide some theoretical bases for the optimal design and operation of practical DC-SOFC-based combined systems.

2. Model description

The DC-SOFC consists of an electrolyte, two electrodes and gas channels, as schematically shown in Fig. 2 (a). The anode and cathode of the DC-SOFC are fed with the solid carbon and air, respectively. In the anode chamber, CO_2 is generated by the chemical reaction between the initial O_2 and solid carbon, and then CO_2 further reacts with solid carbon to produce CO through the Boundouard reaction, i.e., $C+CO_2 \rightarrow 2CO$. The produced CO diffuses into the anode and reacts with O^{2-} to generate CO_2 and electrons, i.e., $CO+O^{2-} \rightarrow CO_2+2e^-$. The generated CO_2 diffuses back into the anode chamber to continuously gasify the carbon and generate CO through the Boundouard reaction. The electrons flow through the external circuit to the cathode, where O_2 is reduced into O^{2-}, i.e., $O+2e^- \rightarrow O^{2-}$. The energy flow diagram of the DC-SOFC/TPVC combined system is schematically given in Fig. 2 (b). It is seen that the proposed system consists of a DC-SOFC, an external heat source, a regenerator, and a TPVC, where

93 the TPVC is composed of a plate radiator and a PV cell with a back surface reflector (BSR) separated by a
94 vacuum gap. When the DC-SOFC operates at low current densities, it requires some heat from the external
95 heat source to maintain the operating temperature. As the current density increases, the increasing heat
96 generated in the DC-SOFC may exceed the heat required by the Boundouard reaction. In this situation, a
97 part of the waste heat is rejected to the environment, and the rest waste heat can be collected and then
98 transferred to the radiator of the TPVC which emits the tailored spectrum to the PV cell and thus the PV
99 cell produces the additional electric power. The heat and mass transfer processes at large current densities
100 are displayed in Fig. 2(c). In Fig. 2 (b), Q_{e} is the heat flow from the external heat source to the DC-SOFC,
101 Q is the heat flow released from the DC-SOFC, Q_{in} is the heat flow released to the radiator, Q_{L} is the
102 heat flow dissipated into the ambient, Q_{r} is the net heat flow from the radiator to the PV cell, Q_0 is the
103 heat flow from the PV cell to the ambient, P_{fc} and P_{tc} are, respectively, the power outputs of the
104 DC-SOFC and TPVC, T_{fc}, T_{r} and T_{tc} are, respectively, the temperatures of the DC-SOFC, radiator and
105 PV cell. The regenerator acts as a heat exchanger to preheat the inlet reactants using the high-temperature
106 outlet products. It has been proved that the outlet products have enough heat to make the inlet reactants
107 reach the operating temperature of the DC-SOFC [23].

108 In Fig. 2 (b), the net heat released from the DC-SOFC can be expressed as

109 $$Q = Q_{\mathrm{t}} - Q_{\mathrm{b}}, \tag{1}$$

110 where $Q_{\mathrm{t}} = \left[-T_{\mathrm{fc}}\Delta S/(2F) + (V_{\mathrm{act}} + V_{\mathrm{ohm}})\right] J_{\mathrm{fc}}$ is the heat released from the electrochemical reaction and
111 overpotential losses, Q_b is the heat required by the Boudouard reaction, F is the Faraday's constant,
112 $J_{\mathrm{fc}} = j_{\mathrm{fc}} S_{\mathrm{fc}}$ is the electrical current, j_{fc} is the current density, S_{fc} is the electrode area, and ΔS is the
113 entropy change of the electrochemical reactions. The activation overpotential V_{act} and the ohmic
114 overpotential V_{ohm} are, respectively, governed by the Butler-Volmer equation and the Ohm's law [25]

$$j_{\mathrm{fc}} = j_0\left[\exp\left(\frac{\alpha nFV_{\mathrm{act}}}{RT_{\mathrm{fc}}}\right) - \exp\left(\frac{(1-\alpha)nFV_{\mathrm{act}}}{RT_{\mathrm{fc}}}\right)\right], \tag{2}$$

and

$$j_{\mathrm{fc}} = -\sigma^{\mathrm{ec}}\nabla(\phi), \tag{3}$$

where j_0 is the exchange current density, α is the electron transfer coefficient, n is the number of transferred electron per electrochemical reaction, R is the universal gas constant, σ^{ec} is the effective conductivity, and ϕ is the ion conducting and electron conducting electric potential.

Gas transfer in the porous electrodes includes free molecular diffusion and Knudsen diffusion, which can be described by the extended Fick's law [26],

$$N_i = -\frac{1}{RT_{\mathrm{fc}}}\left(\frac{B_0 y_i p}{\mu}\frac{\partial p}{\partial z} - D_i\frac{\partial(y_i p)}{\partial z}\right), \quad (i = 1,....,m), \tag{4}$$

where p is the operating pressure of the DC-SOFC, B_0 is the permeability coefficient, y_i is the molar fraction of component i, D_i is the total effective diffusion coefficient of species i $(i = \mathrm{CO}, \mathrm{O_2}$ or $\mathrm{CO_2})$, and z is the direction along gas inlet.

Considering the porous electrodes and the anode chamber, the momentum conservation of gas in the DC-SOFC can be described by the modified Navier-Stokes equation [13]

$$\rho\frac{\partial u}{\partial t} + \rho u\nabla u = -\nabla p + \nabla\left[\mu\left(\nabla u + (\nabla u)^{T_{\mathrm{fc}}}\right) - \frac{2}{3}\mu\nabla u\right] - \frac{\varepsilon\mu u}{k}, \tag{5}$$

where ρ is the gas density, μ is the dynamic viscosity of fluid, u is the velocity vector, and ε is the porosity of the electrode. The above governing equations in DC-SOFCs are solved by the finite element method in COMSOL MULTIPHSICS, more detailed information can be found in Ref. [13].

The output voltage, V, can be expressed as

$$V = E - V_{\mathrm{act}} - V_{\mathrm{ohm}}, \tag{6}$$

where $E = 1.46713 - 0.0004527T_{\mathrm{fc}} + \left[RT_{\mathrm{fc}}/(2F)\right]\ln\left[p_{\mathrm{CO}}\sqrt{p_{\mathrm{O_2}}}/p_{\mathrm{CO_2}}\right]$ is the equilibrium potential [26]

and $p_i\left(i=\mathrm{CO},\mathrm{O}_2,\mathrm{CO}_2\right)$ is the gas partial pressure.

The power output of the DC-SOFC is given by

$$P_{\mathrm{fc}}=VJ_{\mathrm{fc}}. \tag{7}$$

The heat released to the radiator can be expressed as

$$Q_{\mathrm{in}}=Q-Q_L, \tag{8}$$

where $Q_{\mathrm{L}}=S_{\mathrm{L}}[k_L(T_{\mathrm{fc}}-T_0)+\zeta\delta(T_{\mathrm{fc}}{}^4-T_0^4)]$ is heat flow dissipated into the ambient, k_L is the heat conductivity coefficient, $S_{\mathrm{L}}=S_{\mathrm{fc}}-S_{\mathrm{r}}$ is the heat loss area of the DC-SOFC, S_{r} is the front area of the radiator of the TPVC, δ is the Stefan-Boltzmann constant, and ζ is the emissivity of the DC-SOFC.

It is assumed that the characteristic wavelength of thermal radiation is less than the distance between the radiator and the PV cell. Therefore, the heat radiation from the radiator to the PV cell is governed by the Planck' law. Photons emitted from the radiator with energy above the band gap energy are absorbed by the PV cell, and the rest photons are reflected back to the radiator by the BSR. Moreover, the PV cell emits photons to the radiator due to the radiation recombination. Datas and Algora detailedly derived the net heat flow Q_{r} from the radiator to the PV cell as [27, 28]

$$Q_{\mathrm{r}}=\frac{1}{4\pi^2\hbar^3c^2}\left(\begin{array}{l}\displaystyle\int_0^{\infty}\frac{\xi^3}{\exp\left[\xi/(k_{\mathrm{B}}T_{\mathrm{r}})\right]-1}d\xi-f_{\mathrm{rt}}\int_{\xi_g}^{\infty}\frac{\xi^3}{\exp\left[\left(\xi-eV_{\mathrm{tc}}\right)/(k_{\mathrm{B}}T_{\mathrm{tc}})\right]-1}d\xi\\ \displaystyle-\frac{S_{\mathrm{r}}}{S_{\mathrm{tc}}}\frac{rf_{\mathrm{rt}}^2}{1-rf_{\mathrm{tt}}}\int_0^{\xi_g}\frac{\xi^3}{\exp\left[\xi/(k_{\mathrm{B}}T_{\mathrm{r}})\right]-1}d\xi\end{array}\right)S_{\mathrm{tc}}, \tag{9}$$

where the first term of Eq. (9) represents the heat flow emitted from the radiator to the PV cell due to the thermal radiation, the second term indicates the heat flow emitted from the PV cell to the radiator due to the radiation recombination, and the last term is the heat flow reflected from the BSR to the radiator. c is the light speed, $\hbar$ is the reduced Planck constant, k_{B} is the Boltzmann constant, ξ_g is the band-gap energy of the semiconductor material, e is the elementary charge, V_{tc} is the voltage output of the TPVC, f_{rt} is the emitter-to-cell view factor, f_{tt} is the cell-to-cell view factor, r is the reflectivity of the

PV-BSR interface, and S_{tc} is the area of the PV cell. The areas of the radiator and the PV cell are assumed to be the same, and the radiator is supposed as a blackbody.

The current density j_{tc} generated by the TPVC, determined by the difference between the incoming photon flux and outgoing photon flux, can be expressed as [27, 28]

$$j_{tc}=\frac{e}{4\pi^2\hbar^3c^2}\begin{pmatrix}\dfrac{S_r}{S_{tc}}f_{rt}\displaystyle\int_{\xi_g}^{\infty}\frac{\xi^2}{\exp\left[\xi/(k_BT_r)\right]-1}dE-\left(1-f_{tt}\right)\int_{\xi_g}^{\infty}\frac{\xi^2}{\exp\left[\left(\xi-eV_{tc}\right)/(k_BT_{tc})\right]-1}d\xi\\ -\Re^2\left(1-r\right)\displaystyle\int_{\xi_g}^{\infty}\frac{\xi^2}{\exp\left(\left(\xi-eV_{tc}\right)/(K_BT_{tc})\right)-1}d\xi\end{pmatrix}, \tag{10}$$

where $\Re$ is the refraction index of the PV cell.

Thus, the power output of the TPVC, P_{tc}, can be derived as

$$\begin{aligned}P_{tc}&=V_{tc}j_{tc}S_{tc}\\&=V_{tc}\frac{e}{4\pi^2\hbar^3c^2}\begin{pmatrix}\dfrac{S_r}{S_{tc}}f_{rt}\displaystyle\int_{\xi_g}^{\infty}\frac{\xi^2}{\exp\left[\xi/(k_BT_r)\right]-1}d\xi-\left(1-f_{tt}\right)\int_{\xi_g}^{\infty}\frac{\xi^2}{\exp\left[\left(\xi-eV_{tc}\right)/(k_BT_{tc})\right]-1}d\xi\\ -\Re^2\left(1-r\right)\displaystyle\int_{E_g}^{\infty}\frac{\xi^2}{\exp\left[\left(\xi-eV_{tc}\right)/(k_BT_{tc})\right]-1}d\xi\end{pmatrix}S_{tc}.\end{aligned} \tag{11}$$

Neglecting the heat-transfer losses between the DC-SOFC and the radiator of the TPVC, we have

$$Q_r=Q_{in}. \tag{12}$$

Combining Eqs. (8), (9), and (12) yields

$$\begin{aligned}&Q_r-\left(1-\beta\right)[k_L(T_{fc}-T_0)+\zeta\delta(T_{fc}^4-T_0^4)]\\&=\frac{1}{4\pi^2\hbar^3c^2}\begin{pmatrix}\displaystyle\int_0^{\infty}\frac{\xi^3}{\exp\left[\xi/(k_BT_r)\right]-1}d\xi-f_{rt}\int_{\xi_g}^{\infty}\frac{\xi^3}{\exp\left[\left(\xi-eV_{tc}\right)/(k_BT_{tc})\right]-1}d\xi\\ -\dfrac{S_r}{S_{tc}}\dfrac{rf_{rt}^2}{1-rf_{tt}}\displaystyle\int_0^{\xi_g}\frac{\xi^3}{\exp\left[\xi/(k_BT_r)\right]-1}d\xi\end{pmatrix}\beta,\end{aligned} \tag{13}$$

where $\beta=S_{tc}/S_{fc}$ is the area ratio and $\zeta\delta T_0^3/k_L=1.5$.

When the excessive waste heat rejected from the DC-SOFC is recovered by the TPVC, the power output P and efficiency η of the combined system can be, respectively, given by

$$P=P_{fc}+P_{tc}=V_{fc}j_{fc}S_{fc}+V_{tc}j_{tc}S_{tc} \tag{14}$$

and

$$\eta = \frac{P}{P_{\mathrm{fc}} + |Q|} = \frac{V_{\mathrm{fc}} j_{\mathrm{fc}} + V_{\mathrm{tc}} j_{\mathrm{tc}} \beta}{P_{\mathrm{fc}}^{*} + |Q^{*}|}, \tag{15}$$

where $P_{\mathrm{fc}}^{*} = P_{\mathrm{fc}} / S_{\mathrm{fc}}$ and $Q^{*} = Q / S_{\mathrm{fc}}$.

3. Results and discussion

Based on the above formulated model and the parameters summarized in Table 1 [12, 13, 23] and Table 2 [28], the comparison between the modeling results and the experimental data for the DC-SOFC is shown in Fig. 3, where $T_{\mathrm{fc}} = 1073\mathrm{K}$ and more details can be found in Ref. [29]. It is observed that the difference between the modeling results and the experimental data is very small. This indicates that the adopted DC-SOFC model can be used to accurately predict the performance of the DC-SOFC.

Figure 4 shows the power density and the heat flow density of the DC-SOFC versus the operating current density under different operating temperatures. It is observed that there is a current density $j_{\mathrm{s}} = Q_{\mathrm{t}}^{*} / \left[-T_{\mathrm{fc}} \Delta S / (2F) + (V_{\mathrm{act}} + V_{\mathrm{ohm}}) \right]$ at which Q_{t} is equal to Q_{b} (i.e., $Q = 0$), where $Q_{\mathrm{t}}^{*} = Q_{\mathrm{t}} / S_{\mathrm{fc}}$. In this situation, the DC-SOFC can be thermally self-sustained without absorbing or releasing any heat. When $j_{\mathrm{fc}} < j_{\mathrm{s}}$ (i.e., $Q_{\mathrm{t}} < Q_{\mathrm{b}}$), an amount of heat $|Q|$ should be provided to ensure the DC-SOFC normal operation from the external heat source. When $j_{\mathrm{fc}} > j_{\mathrm{s}}$, the heat flow released from the DC-SOFC increases with the increase of j_{fc}, while the power density of the DC-SOFC first increases and then decreases as j_{fc} increases. With a further increase in j_{fc}, the heat flow density Q^{*} increases to equal the power output density P_{fc}^{*} at the current density j_{q}. In this situation, a half of chemical energy in fuel is converted into waste heat rather than power. When $j_{\mathrm{fc}} > j_{\mathrm{q}}$, the Q^{*} will be larger than P_{fc}^{*}. Thus, it is worthwhile to harvest the waste heat released from the DC-SOFC for further power generation. Furthermore, the operating temperature is an important factor that affects the DC-SOFC performance. It is seen from Fig. 4 that P_{fc}^{*}, j_{s}, and j_{q} increase while Q^{*} decreases as the operating temperature

increases.

By using Eq. (14), the area ratio between the DC-SOFC and the TPV cell can be solved for a given j_{fc} and V_{tc} so that the power output and the efficiency of the combined system can be determined. Combining Eqs. (14)-(16), we can generate the three-dimensional graphs of the power output density of the combined system $P^* = P/S_{fc}$ and efficiency η versus j_{fc} and V_{tc}, as shown in Fig. 5. When the TPVC is operated in the small voltage range, P_{tc}^* and η_{tc} are increased with the increase of V_{tc}. When the TPVC is operated at higher voltages, the radiation recombination rises significantly, and consequently, both the power output and the efficiency decrease. As a result, both P^* and η first increase and then decrease with the increasing output voltages. Furthermore, P^* also first increases and then decreases as j_{fc} increases while η is a monotonic decreasing function of j_{fc}.

The power output densities and efficiencies of the combined system, DC-SOFC, and TPVC are compared in Fig. 6, where V_{tc} has been optimized, and j_b is the current density from which the TPVC starts to deliver electricity. It is seen that both P^* and η are always larger than P_{fc}^* and η_{fc} when $j_{fc} > j_b$. When $j_{fc} \le j_b$, the TPVC does not involve in the electricity generation, and P^* and η are equal to P_{fc}^* and η_{fc}. Numerical calculations show that $P_{fc,m}^*$ is 0.477 W cm^{-2}, while P_m^* can reach up to 0.745W cm^{-2}. P_m^* is 56.2% larger than $P_{fc,m}^*$. Moreover, η_p reaches 0.532, which is higher than $\eta_{fc,p}$ of 0.506. Fig. 6 indicates that the proposed combined system is effective in exploiting the heat released from the DC-SOFC.

The temperature of the DC-SOFC is an important parameter for the combined system because it affects the performance of the DC-SOFC as well as the TPVC. The impact of the DC-SOFC operating temperature on P^* and η is shown in Fig. 7. When $j_{fc} > j_b$, the operating temperature positively affects P^* and η since the higher operating temperature improves both the performance of the

DC-SOFC and the TPVC. Both j_s and j_b are shifted rightward as the operating temperature increases because the DC-SOFC releases more heat at a lower working temperature. When $j_{fc} > j_p$, the decrease in the power density contributed by the DC-SOFC is less than the increase in the power density contributed by the TPVC with an increasing j_{fc}, and therefore, P_m^* appears at a current density much larger than j_p. The effects of the operating temperature on P^* and η become more prominent as j_{fc} increases.

The distance between the carbon layer and anode is closely associated with the fuel concentration and solid carbon consumption of the DC-SOFC and thus it affects the performance of the DC-SOFC as well as the combined system. The effect of the distance between the carbon layer and anode on P^* and η is shown in Fig. 8. It is found from Fig. 8 that both P^* and η are enhanced when the distance between the carbon layer and anode is decreased. This is because a decrease in the distance enhances the fuel concentration, yielding an increase in the power density. Moreover, the effect of the distance on P^* and η becomes more significant as j_{fc} increases.

The band-gap energy of the PV cell affects the short-circuit current and open-circuit voltage of the PV cell and thus it affects the performance of the TPVC. The effects of the band-gap energy of the PV cell on P^* and η are shown in Fig. 9. When $j_{fc} > j_b$, it is seen that both P^* and η first increase and then decrease as the band-gap energy ξ_g increases. P^* and η can be optimized by choosing PV cell materials with proper band-gap energy. This is because the open-circuit voltage is raised while the photons absorbed by the PV cell and the short-circuit current are decreased as the band-gap energy increases. Moreover, the effect of the band-gap energy on P^* and η becomes more significant with the increase of j_{fc} as more heat is released from the DC-SOFC. For the typical parameters given in Table 1 and Table 2, the maximum power density of the DC-SOFC/TPVC combined system and the corresponding parameters are given in Table 3.

239 The heat released from the DC-SOFC can be harvested by other heat-to-power devices, such as
240 Stirling cycle [23] and Otto heat engine [24]. The maximum attainable power densities of the
241 DC-SOFC-based combined systems and the corresponding efficiencies are compared in Table 4 at 1123 K.
242 The maximum power density and the corresponding efficiency of the proposed combined system are larger
243 than that of the DC-SOFC/Otto heat engine combined system, whereas they are less than that of the
244 DC-SOFC/Stirling heat engine combined system. Compared with the Stirling heat engine, the unique
245 solid-state TPVC exhibits many other merits such as compact, less auxiliary equipment, no working
246 substance, and no moving parts. With the rapid development of TPVCs, the experimentally measured
247 energy efficiency of ~24% has been already reported [21, 30]. Therefore, the TPVC can be treated as a
248 promising alternative approach to harvest the waste heat from the DC-SOFC.

249 ## 4. Conclusions

250 A combined system is put forwarded to harvest the possible waste heat from the DC-SOFC using the
251 emerging TPVC. Based on the previous 2D tubular DC-SOFC model and the irreversible TPVC model, the
252 mathematical expressions of the power density and efficiency of the combined system are derived. The
253 thermodynamic characteristics of the DC-SOFC have been given and how to operate the combined system
254 is demonstrated. It is found that the proposed combined system is feasible and effective in harvesting the
255 heat released from the DC-SOFC for additional electricity generation. The maximum power density of the
256 combined system with respect to the DC-SOFC alone is approximately increased by 56.2%. Moreover, the
257 efficiency at the maximum power density of the combined system is significantly larger than the efficiency
258 at the maximum power density of the DC-SOFC alone. The higher operating temperature of the DC-SOFC
259 is beneficial to improve both the power density and the efficiency of the combined system. Decreasing the

distance between the carbon layer and anode increases the fuel concentration, resulting in the enhancement of the power density and efficiency. The performance of the combined system can be further improved by properly designing the PV cell with optimum band gap energy. Comparisons show that the performance of the DC-SOFC/TPVC combined system is in the acceptable level. Because of the unique advantages, the TPVCs can be regarded as a potential alternative for the waste recovery from DC-SOFCs.

Although the proposed DC-SOFC/TPVC combined system has large power density and high efficiency, reducing the cost of manufacturing such the system is a key step toward commercialization [31]. Developing high performance radiator of the TPVC and fabrication of efficient catalyst for the DC-SOFC are two biggest challenges in development this technology [10, 32]. Note that the model in this paper is highly simplified, and the assumptions made may affect the actual performance of the combined system. For example, the radiative recombination is considered as the only mechanism losses and the other energy losses are neglected in the TPVC, and the ideal anti-reflective coating is covered with the PV cell so that all incoming photons can penetrate into the PV cell. These assumptions will cause the theoretical performance better than the actual performance.

Acknowledgements

This research is supported by the Natural Science Foundation of Zhejiang Province (Grant No. LQ14E060001), National Natural Science Foundation of China (Grant No. 51406091) and the K. C. Wong Magna Fund in Ningbo University.

281 **Nomenclature**

B_0	Permeability coefficient, m^2
c	Speed of light, $\mathrm{m\,s^{-1}}$
D_i	Total effective diffusion coefficient component i, $\mathrm{m^2\,s^{-1}}$
e	Elementary charge, C
E	Equilibrium potential, V
f_{rt}	Emitter-to-cell view factor,
f_{tt}	Cell-to-cell view factor,
F	Faraday's constant, $\mathrm{C\,mol^{-1}}$
$\hbar$	Reduced Planck constant, J s
j_{fc}	Current density, $\mathrm{A\,m^{-2}}$
j_0	Exchange current density, $\mathrm{A\,m^{-2}}$
J_{fc}	Electrical current, A
k_{B}	Boltzmann constant, $\mathrm{J\,K^{-1}}$
k_L	Heat conductivity coefficient, $\mathrm{W\,m^{-2}\,K^{-2}}$
n	Number of transferred electron per electrochemical reaction,
p_x	Gas partial pressure, Pa
P	Power outputs, W
Q_e	Heat flow from the external heat source to the DC-SOFC, W
Q_b	Heat required by the Boudouard reaction, W
Q	Heat flow released from the DC-SOFC, W
Q_{in}	Heat flow released to the radiator, W
Q_L	Heat flow dissipated to the ambient, W
Q_r	Net heat flow from the radiator to the PV cell, W
Q_0	Heat flow from the PV cell to the ambient, W
r	Reflectivity,
R	Universal gas constant, $\mathrm{J\,mol^{-1}\,K^{-1}}$
$\Re$	Refraction index,
S	Area, m^2
S_{L}	Effective heat leakage area of the DC-SOFC, m^2
ΔS	Entropy change of the electrochemical reactions, $\mathrm{J\,mol^{-1}\,K^{-1}}$
T	Temperature, K
u	Velocity vector, $\mathrm{m^3\,s^{-1}}$

V_{tc}	voltage output of the TPVC, V
V_{act}	Activation overpotential, V
V_{ohm}	Ohmic overpotential, V
y_i	Molar fraction of species i,
z	Direction
Greek letters	
α	Electron transfer coefficient,
β	Area ratio of the DC-SOFC to the PV cell,
δ	Stefan-Boltzmann constant, $\mathrm{W\,m^{-2}\,K^{-4}}$
ε	Porosity of the electrode,
ζ	Emissivity of the DC-SOFC,
μ	Dynamic viscosity of fluid, $\mathrm{Pa\,s}$
ξ_g	Band gap energy, eV
ρ	Density, $\mathrm{Kg\,m^{-3}}$
σ^{ec}	Effective conductivity, $\mathrm{S\,m^{-1}}$
ϕ	Electric potential, V
Subscripts	
i	species $\left(i = \mathrm{CO}, \mathrm{O_2}\ \text{or}\ \mathrm{CO_2}\right)$
r	Radiator
fc	Fuel cell
tc	Thermophotovoltaic cell
Abbreviation	
DC-SOFC	Direct carbon solid oxide fuel cell
DCFC	Direct carbon fuel cell
TPVC	Thermophotovoltaic cell
BSR	Back surface reflector

References

[1] Kohse-Höinghaus K, Reimann M, Guzy J. Clean combustion: Chemistry and diagnostics for a systems approach in transportation and energy conversion. Prog Energy Combust Sci 2018; 65: 1-5.

[2] Lee K S, Spendelow J S, Choe Y K, Fujimoto C, Kim Y S. An operationally flexible fuel cell based on quaternary ammonium-biphosphate ion pairs. Nat Energy, 2016, 1: 16120.

[3] Das V, Padmanaban S, Venkitusamy K, Selvamuthukmaran R, Blaabjerg F, Siano P. Recent advances and challenges of fuel cell based power system architectures and control–A review. Renew Sustain Energy Rev 2017; 73: 10-18.

[4] Pachauri R K, Chauhan Y K. A study, analysis and power management schemes for fuel cells. Renew Sustain Energy Rev 2015; 43: 1301-1319.

[5] Park S, Vohs J M, Gorte R J. Direct oxidation of hydrocarbons in a solid-oxide fuel cell. Nature 2000; 404: 265-267.

[6] Cao T, Huang K, Shi Y, Cai N. Recent advances in high-temperature carbon–air fuel cells. Energy Environ Sci 2017; 10: 460-490.

[7] Jiang C, Ma J, Corre G, Jain S L, Irvine J T S. Challenges in developing direct carbon fuel cells. Chem Soc Rev 2017; 46: 2889-2912.

[8] Johnson D U, Mitchell R E, Gür T M. Modeling Power Production in a Tubular Carbon Fuel Cell. ECS Trans 2014; 61: 235-243.

[9] Tang Y, Liu J. Effect of anode and Boudouard reaction catalysts on the performance of direct carbon solid oxide fuel cells. Int J Hydrogen Energy 2010; 35: 11188-11193.

[10] Li C, Shi Y, Cai N. Performance improvement of direct carbon fuel cell by introducing catalytic gasification process. J Power Sources 2010; 195: 4660-4666.

309 [11] Jewulski J, Skrzypkiewicz M, Struzik M, Radziejewska-Lubarska L. Lignite as a fuel for direct carbon
310 fuel cell system. Int J Hydrogen Energy 2014; 39: 21778-21785.
311 [12] Xu H, Chen B, Liu J, Ni M. Modeling of direct carbon solid oxide fuel cell for CO and electricity
312 cogeneration. Appl Energy 2016; 178: 353-362.
313 [13] Xu H, Chen B, Zhang H, Kong W, Liang B, Ni M. The thermal effect in direct carbon solid oxide fuel
314 cells. Appl Therm Eng 2017; 118: 652-662.
315 [14] Wu S, Zhang H, Ni M. Performance assessment of a hybrid system integrating a molten carbonate
316 fuel cell and a thermoelectric generator. Energy 2016; 112: 520-527.
317 [15] Huang C, Pan Y, Wang Y, Su G, Chen J. An efficient hybrid system using a thermionic generator to
318 harvest waste heat from a reforming molten carbonate fuel cell. Energy Convers Managem 2016; 121:
319 186-193.
320 [16] Yang Z, Peng W, Liao T, Zhao Y, Lin G, Chen J. An efficient method exploiting the waste heat from a
321 direct carbon fuel cell by means of a thermophotovoltaic cell. Energy Convers Managem 2017; 149:
322 424-431.
323 [17] Rokni M. Performance comparison on repowering of a steam power plant with gas turbines and solid
324 oxide fuel cells. Energies 2016; 9: 399.
325 [18] De Escalona J M M, Sánchez D, Chacartegui R, Sánchez T. Performance analysis of hybrid systems
326 incorporating high temperature fuel cells and closed cycle heat engines at part-load operation. Int J
327 Hydrogen Energy 2013; 38: 570-578.
328 [19] Baronci A, Messina G, McPhail S J, Moreno. Numerical investigation of a MCFC (Molten Carbonate
329 Fuel Cell) system hybridized with a supercritical CO_2 Brayton cycle and compared with a bottoming
330 Organic Rankine Cycle. Energy 2015; 93: 1063-1073.

[20] Rokni M.Thermodynamic analysis of an integrated solid oxide fuel cell cycle with a rankine cycle. Energy Convers Managem 2010; 51: 2724-2732.

[21] Datas A, Martí A. Thermophotovoltaic energy in space applications: Review and future potential. Sol Energy Mater Sol Cells 2017; 161: 285-296.

[22] Yang Z, Liao T, Zhou Y, Lin G, Chen J. Performance evaluation and parametric optimum design of a molten carbonate fuel cell-thermophotovoltaic cell hybrid system. Energy Convers Managem 2016; 128: 28-33.

[23] Xu H, Chen B, Tan P, Zhang H, Yuan J, Liu J, Ni M. Performance improvement of a direct carbon solid oxide fuel cell system by combining with a Stirling cycle. Energy 2017; 140: 979-987.

[24] Xu H, Chen B, Tan P, Zhang H, Yuan J, Irvine J T S, Ni M. Performance improvement of a direct carbon solid oxide fuel cell through integrating an Otto heat engine. Energy Convers Managem 2018; 165: 761-770.

[25] Ni M. Modeling and parametric simulations of solid oxide fuel cells with methane carbon dioxide reforming. Energy Convers Managem 2013; 70: 116-129.

[26] Andersson M, Yuan J, Sundén B. Review on modeling development for multiscale chemical reactions coupled transport phenomena in solid oxide fuel cells. Appl Energy 2010; 87: 1461-1476.

[27] Datas A, Algora C. Detailed balance analysis of solar thermophotovoltaic systems made up of single junction photovoltaic cells and broadband thermal emitters. Sol Energy Mater Sol Cells 2010; 94: 2137-2147.

[28] Datas A, Algora C. Global optimization of solar thermophotovoltaic systems. Prog Photovoltaics Res Appl 2013; 21: 1040-1055.

[29] Xie Y, Cai W, Xiao J, Tang Y, Liu J, Liu M. Electrochemical gas–electricity cogeneration through

353 direct carbon solid oxide fuel cells. J Power Sources 2015; 277: 1-8.

354 [30] Wernsman B, Siergiej RR, Link SD, Mahorter RG, Palmisiano MN, Wehrer RJ, Schultz R W,

355 Schmuck G P, Messham R L, Murray S, Murray C S, Newman F, Taylor D, DePoy D M, Rahmlow T.

356 Greater than 20% radiant heat conversion efficiency of a thermophotovoltaic radiator/module system using

357 reflective spectral control. IEEE Trans Electron Devices 2004; 51: 512-515.

358 [31] Van der Heide J, Posthuma N E, Flamand G, Poortmans J. Development of low‐cost

359 thermophotovoltaic cells using germanium substrates. AIP Conf Proc 2007; 890 (1): 129-138.

360 [32] Nam Y, Yeng Y X, Lenert A, Bermel P, Celanovic I, Soljačić M, Wang E N. Solar thermophotovoltaic

361 energy conversion systems with two-dimensional tantalum photonic crystal absorbers and emitters. Sol

362 Energy Mater Sol Cells 2014; 122: 287-296.

363

364

List of Tables

373

Table 1. Parameters used in the DC-SOFC model [12, 13, 23].

Parameters	Value or expression	Unit
Ionic conductivity		
σ_{GDC}	$\frac{100}{T}\times 10^{\left(6.66071-\frac{5322.92}{T}\right)}$	S m^{-1}
σ_{YSZ}	$3.34\times 10^{4}\,\mathrm{e}^{\frac{-10300}{T}}$	S m^{-1}
Electronic conductivity		
σ_{silver}	$\frac{1.59\times 10^{8}}{0.0038T-0.1134}$	S m^{-1}
Porosity		
$\varepsilon_{\mathrm{an}}$	0.46	
$\varepsilon_{\mathrm{ca}}$	0.46	
Electrode volume fraction		
V_{GDC}	0.21	
V_{silver}	0.79	
TPB length of electrode		
Anode	2.14×10^{5}	m^{2} m^{-3}
Cathode	2.14×10^{5}	m^{2} m^{-3}
Tortuosity		
τ_{an}	3	
τ_{ca}	3	

Exchange current density		
i_0^{CO}	450	A m^{-2}
$i_0^{O_2}$	400	A m^{-2}
Charge transfer coefficient		
α_{CO}	0.5	
α_{O_2}	0.5	
Equilibrium constant of Boudouard reaction	$k_{rb} = 6 \times 10^{13}$	1/s
Activation energy of Boudouard reaction	$E_{rb} = 248$	KJ mol^{-1}

374

375

376

Table 2. Parameters used in the TPVC model [28].

Parameters	**Value**
Temperature of the PV cell, K	310
Radiator-to-cell view factor	1
Cell-to-cell view factor	0
Reflectivity of the PV- BSR interface,	0.9
Refraction index of the PV cell,	3.5

377

378

379 Table 3. The maximum power density of the DC-SOFC/TPVC combined system and the corresponding

380 parameters at $T_{\mathrm{fc}}=1123\mathrm{K}$.

$P_{\mathrm{m}}^{*}\left(\mathrm{W cm^{-2}}\right)$	η_{P}	$d\ (\mu\mathrm{m})$	$\xi_g\ (\mathrm{eV})$	β	$j_{\mathrm{p}}\left(\mathrm{A/cm^{2}}\right)$	$V_{\mathrm{tc}}\ (\mathrm{V})$
0.745	0.532	59	0.35	0.196	3.55	0.220

381

382

383 Table 4. Performance comparisons of several DC-SOFC-based combined systems at 1123K.

Combined system	$P_{\mathrm{m}}^{*}\left(\mathrm{W\,cm^{-2}}\right)$	η_{P}
DC-SOFC/TPVC	0.745	0.532
DC-SOFC/Strling heat engine [23]	0.949	0.655
DC-SOFC/Otto heat engine [24]	0.696	0.501

384

385

Figure captions:

Fig. 1. Maximum power density improvement comparison of the different waste heat technologies for MCFCs [22], where $u=\left[\left(P_{\mathrm{m}}^{*}-P_{\mathrm{m,f}}^{*}\right)/P_{\mathrm{m,f}}^{*}\right]\times 100\%$, P_{m}^{*} is the maximum power density of the combined system and $P_{\mathrm{m,f}}^{*}$ is the maximum power density of the MCFC.

Fig. 2. The schematic diagrams of (a) the DC-SOFC, (b) the energy flow of the DC-SOFC/TPVC combined system, and (c) the heat and mass transfer processes at large current density.

Fig. 3. Comparison between the modeling results and experimental data.

Fig. 4. The power density and the heat flow density of the DC-SOFC varying the current density under different operating temperatures for $d=59\ \mu\mathrm{m}$ and $\xi_g=0.35\,\mathrm{eV}$, where j_s is the current density at which the heat released from the DC-SOFC is equal to that required by the Boundouard reaction, and j_q is the current density at which the power density is equal to the heat released.

Fig. 5. The (a) power density and (b) efficiency of the combined system versus the current density of the DC-SOFC and voltage output of the TPVC for $T_{\mathrm{fc}}=1123\,\mathrm{K}$, $d=59\ \mu\mathrm{m}$, and $\xi_g=0.35\,\mathrm{eV}$.

Fig. 6. The (a) power densities and (b) efficiencies of the combined system, DC-SOFC and TPVC varying with the current density of the DC-SOFC for $T_{\mathrm{fc}}=1123\,\mathrm{K}$, $d=59\ \mu\mathrm{m}$, and $\xi_g=0.35\,\mathrm{eV}$, where P_{m}^{*} and $P_{\mathrm{fc,m}}^{*}$ are, respectively, the maximum power densities of the combined system and the DC-SOFC, j_{p} and $j_{\mathrm{fc,p}}$ are, respectively, the current densities at the maximum power densities of the combined system and the DC-SOFC, j_{b} is the current density from which the TPVC begins to work, η_{p} and $\eta_{\mathrm{fc,p}}$ are, respectively, the efficiencies corresponding to the maximum power densities of the combined system and the DC-SOFC.

Fig. 7. Effects of the DC-SOFC operating temperature on the (a) power density and (b) efficiency of the combined system for $d=59\ \mu\mathrm{m}$ and $\xi_g=0.35\,\mathrm{eV}$.

Fig. 8. Effects of the distance between the carbon layer and anode on the (a) power density and (b) efficiency of the combined system for $T_{\mathrm{fc}} = 1123\,\mathrm{K}$ and $\xi_g = 0.35\,\mathrm{eV}$.

Fig. 9. Effects of the band gap energy of the TPVC on the (a) power density and (b) efficiency of the combined system for $T_{\mathrm{fc}} = 1123\,\mathrm{K}$ and $d = 59\ \mu\mathrm{m}$.

414 Fig. 1

415

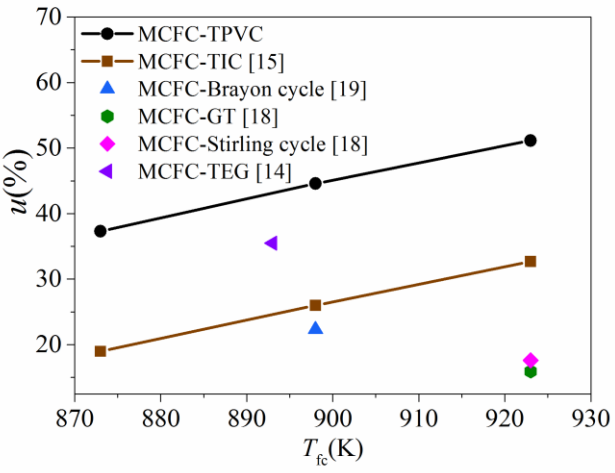

416 Fig. 1. Maximum power density improvement comparison of the different waste heat technologies for

417 MCFCs [22], where $u=\left[\left(P_{\mathrm{m}}^{*}-P_{\mathrm{m,f}}^{*}\right)/P_{\mathrm{m,f}}^{*}\right]\times 100\%$, P_{m}^{*} is the maximum power density of the combined

418 system and $P_{\mathrm{m,f}}^{*}$ is the maximum power density of the MCFC.

419

420

421 Fig. 2.

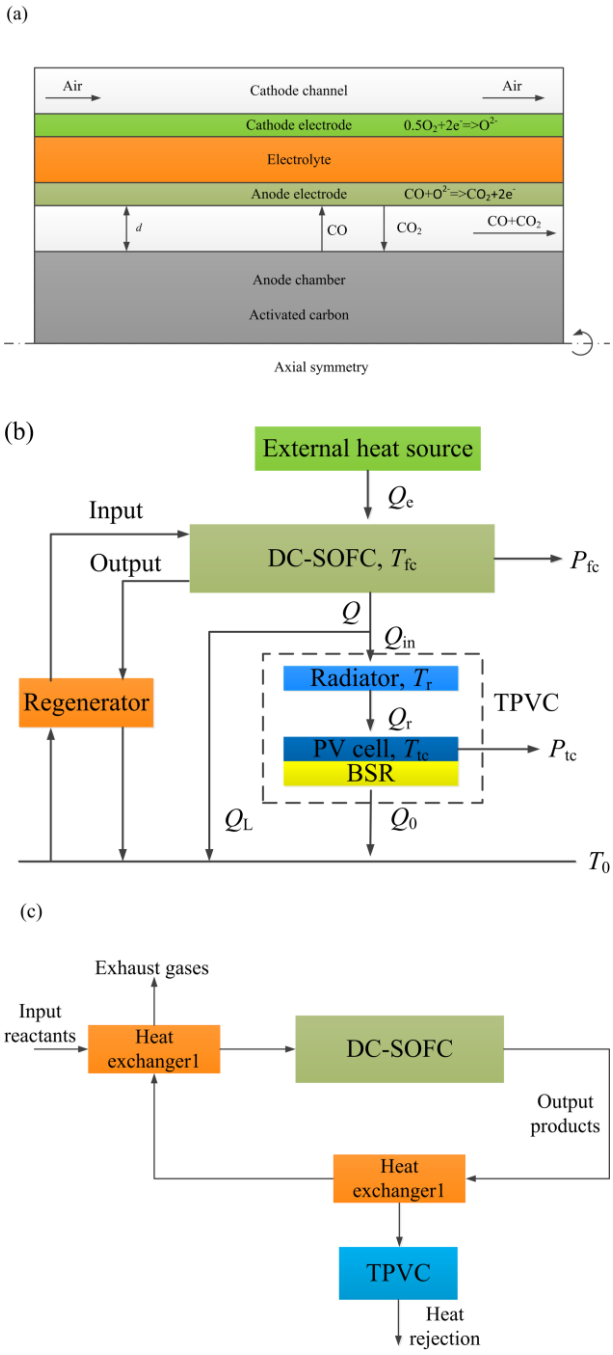

422

423

424

425 Fig. 2. The schematic diagrams of (a) the DC-SOFC, (b) the energy flow of the DC-SOFC/TPVC

426 combined system, and (c) the heat and mass transfer processes at large current density.

427

428

429 Fig. 3.

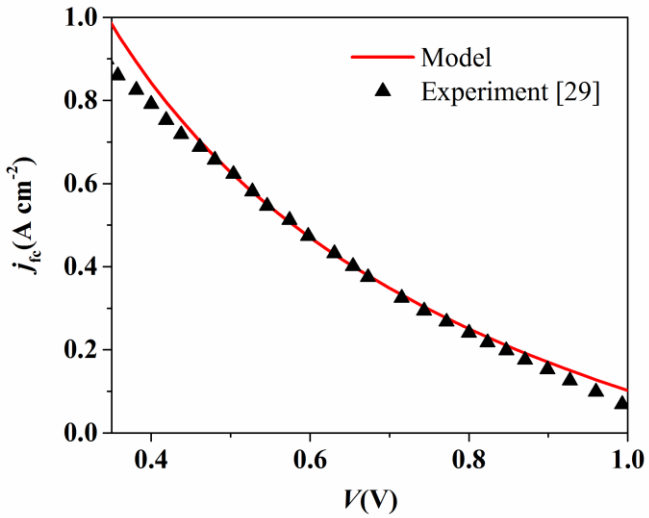

430

431 Fig. 3. Comparison between the modeling results and experimental data.

432

Fig. 4.

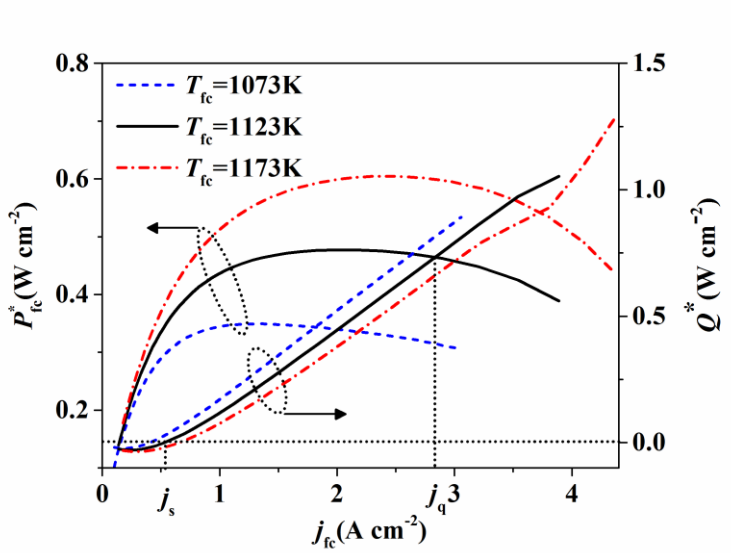

Fig. 4. The power density and the heat flow density of the DC-SOFC varying the current density under different operating temperatures for $d = 59\,\mu\text{m}$ and $\xi_g = 0.35\,\text{eV}$, where j_s is the current density at which the heat released from the DC-SOFC is equal to that required by the Boundouard reaction, and j_q is the current density at which the power density is equal to the heat released.

Fig. 5.

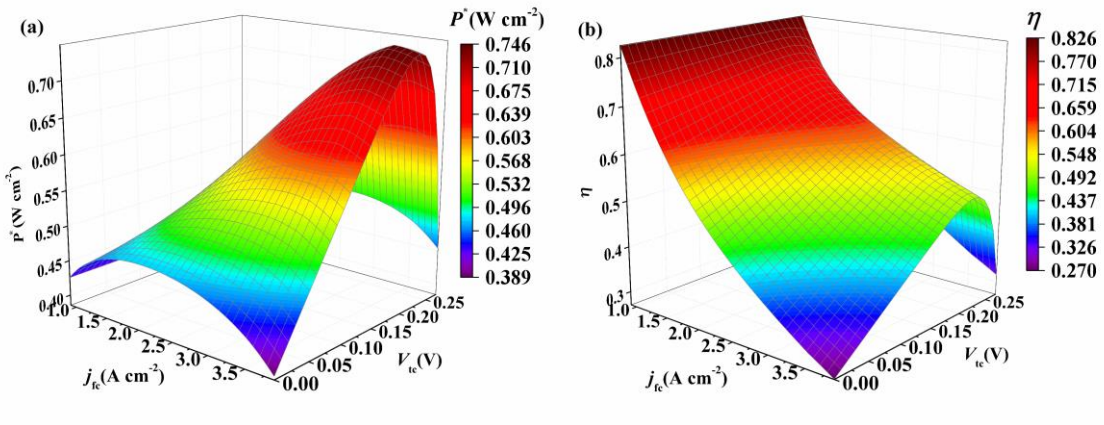

Fig. 5. The (a) power density and (b) efficiency of the combined system versus the current density of the DC-SOFC and voltage output of the TPVC for $T_{fc} = 1123\,\mathrm{K}$, $d = 59\,\mu\mathrm{m}$, and $\xi_g = 0.35\,\mathrm{eV}$.

Fig. 6.

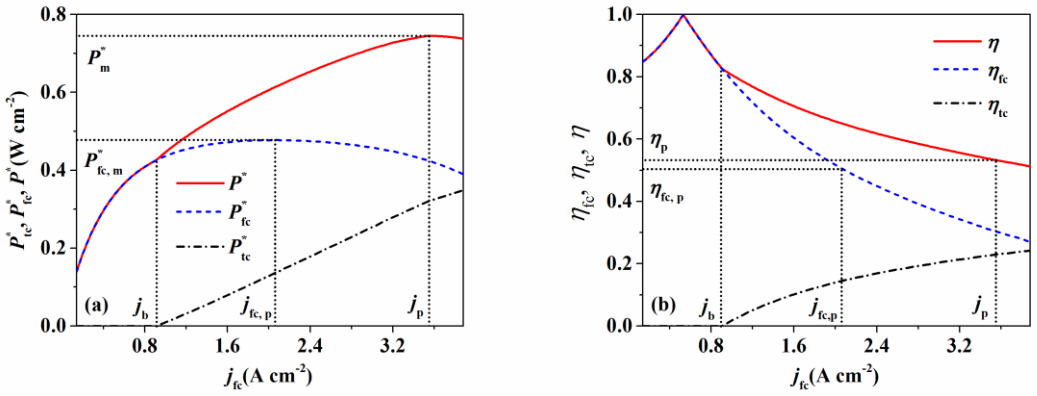

Fig. 6. The (a) power densities and (b) efficiencies of the combined system, DC-SOFC and TPVC varying with the current density of the DC-SOFC for $T_{fc}=1123\,\mathrm{K}$, $d=59\,\mu\mathrm{m}$, and $\xi_g=0.35\,\mathrm{eV}$, where P^*_m and $P^*_{fc,m}$ are, respectively, the maximum power densities of the combined system and the DC-SOFC, j_p and $j_{fc,p}$ are, respectively, the current densities at the maximum power densities of the combined system and the DC-SOFC, j_b is the current density from which the TPVC begins to work, η_p and $\eta_{fc,p}$ are, respectively, the efficiencies corresponding to the maximum power densities of the combined system and the DC-SOFC.

455 Fig. 7.

456

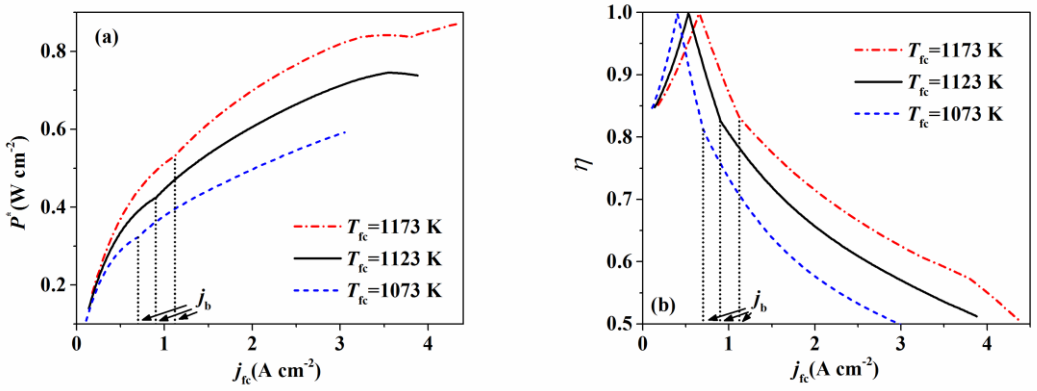

457 Fig. 7. Effects of the DC-SOFC operating temperature on the (a) power density and (b) efficiency of the

458 combined system for $d = 59\ \mu\text{m}$ and $\xi_g = 0.35\,\text{eV}$.

459

460 Fig. 8.

461

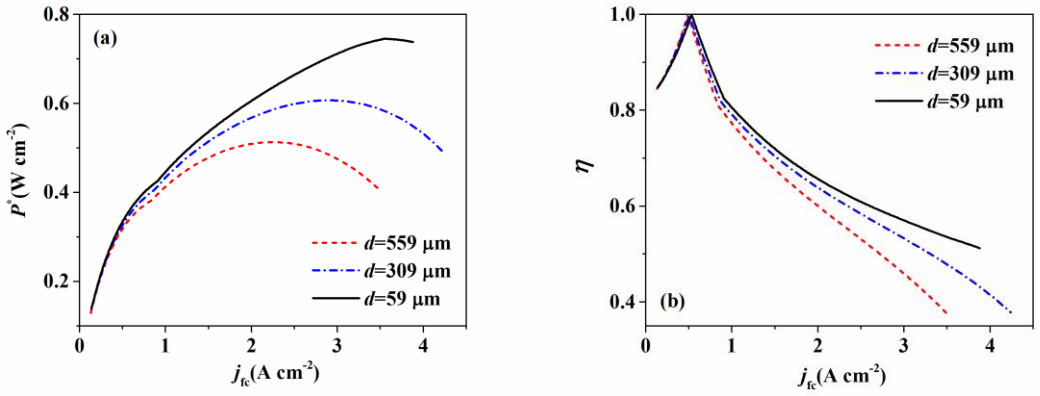

462 Fig. 8. Effects of the distance between the carbon layer and anode on the (a) power density and (b)

463 efficiency of the combined system for $T_{fc} = 1123\,\mathrm{K}$ and $\xi_g = 0.35\,\mathrm{eV}$.

464

Fig. 9.

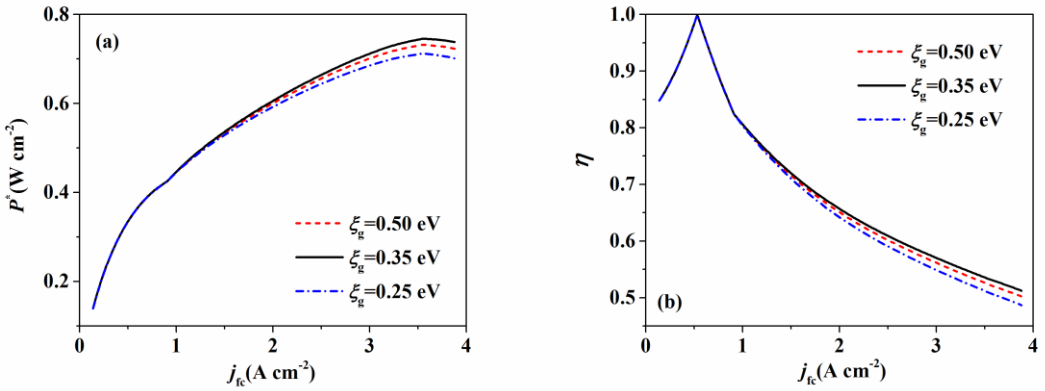

Fig. 9. Effects of the band gap energy of the TPVC on the (a) power density and (b) efficiency of the combined system for $T_{fc} = 1123\,\mathrm{K}$ and $d = 59\,\mu\mathrm{m}$.